Postprint of: Rucka M., Wojtczak E., Knak M., Kurpińska M., Characterization of fracture process in polyolefin fibre-reinforced concrete using ultrasonic waves and digital image correlation, CONSTRUCTION AND BUILDING MATERIALS, Vol. 280 (2021), 122522, DOI: 10.1016/j.conbuildmat.2021.122522

Characterization of fracture process in polyolefin fibre-reinforced concrete using ultrasonic waves and digital image correlation

Magdalena Rucka [1],*, Erwin Wojtczak [1], Magdalena Knak [1] and Marzena Kurpińska [1]

[1] Department of Mechanics of Materials and Structures, Faculty of Civil and Environmental Engineering,
Gdańsk University of Technology, Narutowicza 11/12, 80-233 Gdańsk, Poland,
emails: magdalena.rucka@pg.edu.pl, erwin.wojtczak@pg.edu.pl, s168197@student.pg.edu.pl,
marzena.kurpinska@pg.edu.pl

* corresponding author

Abstract

This study explores the monitoring of the fracture process in concrete beams and aims to characterize the evolution of damage in polyolefin fibre-reinforced concrete beams by utilizing the integrated application of two measurement techniques, digital image correlation and ultrasonic testing. The interpretation of registered wave time histories data was provided by the calculation of the magnitude-phase-composite metrics. An efficient procedure for the determination of strain field and the identification of crack height was subsequently developed. The results of the study show that the energy and phase shifts of ultrasonic waves can be used as autonomous damage indicators in a system for the real-time monitoring of a fracture process.

Keywords

Non-destructive testing; Structural health monitoring; Fibre-reinforced concrete; Ultrasonic waves; Digital image correlation; Crack identification

1. Introduction

Concrete is one of the most widely used building materials. A recent trend in constructional cement-based composites aims for the development of concrete with improved mechanical properties and durability. The integration of additional components with concrete, in the form of fibres or fillers, has attracted considerable interest from researchers. Nanoparticles such as nano-SiO2 and nano-TiO2 [1–4] can effectively fill the voids between cement and silica fume particles and can hence, provide enhanced compressive and flexural strength and durability. Moreover, various micro and macro fibres made of steel, carbon, basalt, glass, or plastic can not only improve static and dynamic properties but also reduce early age micro-cracking of fibre-reinforced concrete [5–7]. Nowadays, polymer fibres have been successfully employed in diverse structural applications like sleepers, overlays, ground supported slabs, or industrial floors. A few recent studies [8–17] have reported a broad range of experimental and numerical investigations focused on the comprehensive mechanical and microstructural evaluation of concrete reinforced with polyethylene, polyolefin, polypropylene, or polyvinyl fibres.

Fracture is one of the most important phenomena than can appear in concrete elements and is closely related to the heterogeneous structure of the material. It is preceded by the formation of micro-cracks, which then transform into macro-cracks that may be acceptable in concrete structures, as long as they do not exceed the width limit according to the design standards. To characterize the concrete behaviour and to ensure the safety of the reinforced concrete structures, early detection of cracks with oversized width in the initial stage of loading is of great interest in civil engineering. Szeląg [18] reviewed the achievements in the field of diagnostics of cracking in cement composites. Accordingly, the four most important aspects related to the evaluation of a cracking pattern can be addressed: (i) the process of crack formation and its evolution into a branched system of cracks; (ii) diagnostic techniques for the digital extraction of the cracking patterns based on image analysis; (iii) quantitative parameters used to describe the degree of development and the morphology of the cracks system; (iv) influence of the cracking pattern on selected properties of cement composites [18]. There are many non-destructive testing (NDT) techniques currently utilized for the evaluation of concrete structures. One of the most developed groups of techniques is utilization of the phenomenon of elastic wave propagation, including acoustic emission (AE) [19–21] and ultrasonic waves (UW) [22–25]. A very promising optical method with several applications in the diagnosis of concrete structures is the digital image correlation (DIC) technique, which is based on the interpretation of digital images of the elements surface under loading [26–28].

Monitoring of the fracture process of the fibre-reinforced cement composites has been widely considered in previous research. Liu et al. [6] investigated the fracture in carbon fibres reinforced coral concrete. They revealed that the use of DIC enabled the characterization of the three phases of the flexural damage process, namely, the micro-crack initiation phase, macro-crack evolution phase, and main crack propagation phase. Skarżyński and Suchorzewski [29] compared the fracture phenomenon in plain concrete and concrete reinforced with steel fibres. The fracture process on the surface of samples was characterized using the DIC method, and that inside the samples by means of X-ray micro-computed tomography. The paper by Picazo et al. [30] deals with the assessment of the shear behaviour of polyolefin fibre-reinforced concrete. The analysis of the cracking processes was performed by using the DIC technique, which correlated the crack initiation and growth process with the shear stress. Francioso et al. [31] evaluated the flexural behaviour of fibre-reinforced cement composites subjected to elevated temperatures with the use of DIC and digital microscopy techniques. Suchorzewski et al. [32] applied DIC to evaluate the cracking of concrete enhanced with multi-wall carbon nanotubes. The resistivity was measured and the results were compared with the crack patterns to explore the possibility of the concrete self-sensing. Fibre-reinforced gypsum was tested by Suárez et al. [33]. They used DIC to characterize the performance of different polymer fibres as reinforcements for gypsum in three-point bending, compression, and pull-out tests. The problem of monitoring the mechanical behaviour of modified cement composites has also been considered with the use of the acoustic emission technique. Aggelis et al. [34] applied acoustic emission for monitoring the mechanical behaviour of concrete with steel fibres. Specific AE indices were proposed to monitor the changes in concrete microstructure. Barkoula et al. [35] monitored the failure processes in nano-silica modified mortar, using the AE technique. They observed that for nano-modified material, AE activity was higher than that for the plain mortar, as a larger number of fracturing incidents occurred without significant changes in the total received energy [35]. Logoń and Schabowicz [36] investigated the destruction process in a number of cement composites with a high volume of polypropylene fibre reinforcement. They used the AE to distinguish the micro-events occurring during a four-point bending tensile test. Rasheed et al. [37] conducted a study on the fracture of synthetic fibre-reinforced cellular concrete. Using AE, they studied the crack initiation and propagation characteristics in notched beams. Logoń [38] analysed the possibility of the application of AE for detecting the failure mechanisms in quasi-brittle concrete with dispersed polypropylene fibres. He noticed that the interpretation of 2D and 3D acoustic spectra could be useful in the identification and description of the failure process in fibre-reinforced concrete elements. Some researchers investigated the simultaneous application of more than one diagnostic method. Rouchier et al. [39] presented a study on developing a methodology for the detection and monitoring of damage in fibre-reinforced mortar. They used DIC and AE during tensile loading tests. An example of integrated application of both AE and DIC on real-scale elements is presented by Zhang et al. [40]. They concluded that AE can detect cracks faster than traditional displacement sensors, and the DIC technique allows the identification of crack propagation in further detail. It is, however, essential to note that the simultaneous application of ultrasonic wave propagation and DIC method to characterize the fracture process in fibre-reinforced concrete has not been extensively investigated.

The main contribution of the study is an investigation of the integrated application of two measurement techniques, i.e. digital image correlation (DIC) and ultrasonic testing (UT). The aim was to analyse the evolution of damage and the possibility of its characterization in a non-invasive manner. Experimental investigations were performed on concrete beams reinforced with macro-synthetic polyolefin fibres with twisted-bundles. The fracture process due to mechanical loading in a three-point bending test was considered. The diagnostic procedure was based on the simultaneous collection of wave propagation signals and photographs of analysed specimens during mechanical degradation. The interpretation of experimental data was provided by calculating the magnitude-phase-composite metrics for the registered wave time histories and DIC for the collected photographs. The novel element of the study is the proposition of using the curvature of the phase error metric to characterise the initial stage of mechanical degradation of the concrete. An attempt for the identification of damage was also made. An efficient procedure for the determination of strain field and the identification and monitoring of crack height was developed. The influence of fibre dosage on the post-cracking behaviour and the possibility of early detection of cracking was analysed.

2. Materials and methods

2.1. Materials and mix design

Water, aggregate, cement, and fibres were used for the production of concrete. The cement used was CEM I 42.5R Portland cement. The chemical composition and physical properties of the cement are shown in Tables 1 and 2, respectively. The fine aggregate used was a natural washed sand with a particle size of 0–2 mm, and a volume density of 2.65

kg/dm^3. Natural pebble aggregate was used as a coarse aggregate with particle sizes of 2–8 mm and 8–16 mm, and a volume density of 2.65 kg/dm^3. The grain distribution of individual types of aggregates as well as of mixture aggregates is presented in Figure 1. The water from the mains was used for the tests. A superplasticiser was added to the concrete mix to achieve good homogeneity and workability.

Table 1. Chemical compositions of cement [wt.%].

Cement type	CaO	SiO_2	Al_2O_3	Fe_2O_3	MgO	Na_2O	K_2O	SO_3	TiO_2	Cl
CEM I 42.5R	63.4	21.7	6.2	3.1	1.0	0.16	0.64	3.9	0.25	0.06

Table 2. Physical properties of cement.

Cement type	Setting start time [min]	Setting end time [min]	Compressive strength [MPa]		Blaine fineness [cm^2/g]	Loss on ignition [%]	Water demand [%]
			after 2 days	after 28 days			
CEM I 42.5R	155	195	30.2	57.3	3504	3.4	27.5

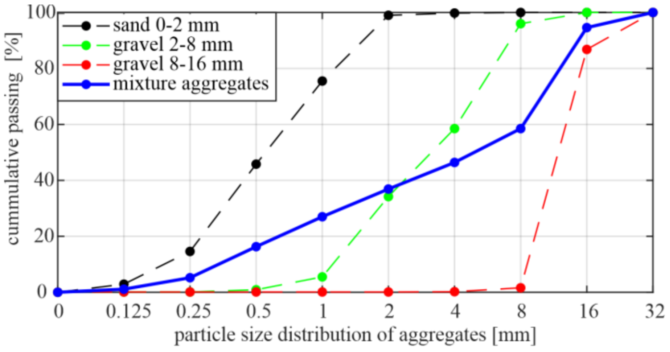

Figure 1. Aggregate grain distribution curves for particles with sizes 0–2 mm, 2–8 mm and 8–16 mm, and the mixture aggregates

The macro polymer fibres were used as reinforcement. The properties of fibres are given in Table 3. The fibres are made of polyolefin and produced as twisted-bundles of a length of 54 mm (Figure 2).

Table 3. Properties of polymer fibres.

Length [mm]	Diameter [mm]	Relative density [g/cm^3]	Number of fibres per 1 kg [pcs.]	Total length of reinforcement [m/kg]
54	0.45	0.91	110 000	5940

Figure 2. Photograph of twisted-bundle macro-polyolefin fibres

Concrete strength class C30/37 was assumed. Granulation of mineral aggregates (Figure 1) was selected such that the mixtures had a good workability. The amounts of concrete mixture components were determined by the analytical–experimental method. In all tests, the same composition of concrete was used: CEM I 42.5R (380 kg/m^3), water (165 kg/m^3), sand 0–2 (648 kg/m^3), gravel 2–8 (426 kg/m^3), gravel 8–16 (754 kg/m^3), polycarboxylate ether (PCE) super-plasticizer (0.8 % of cement content). Four concrete mixtures were produced: one control mixture without fibres (mixture #000) and three mixtures with different contents of macro polymer fibres equal to 2 kg/m^3 (mixture #002), 4 kg/m^3 (mixture #004) and 6 kg/m^3 (mixture #006).

The components of the mixture were mixed using a mechanical mixer. The aggregate and fibres were mixed for 2 min, then the cement, water, and admixtures were added and mixed for another 2 min. Consistency of the all mixtures was within the range of S3 (150 ± 10 mm), and the air content of the concrete mix ranged between 1.9–2.2 %. Compressive strength, determined for the cubic samples with dimensions of 15 x 15 x 15 cm^3 is given in Table 4.

Table 4. Compressive strength of the 15 x 15 x 15 cm^3 cubes

Sample	Compression strength [MPa]
mixture #000	67.2
mixture #002	63.8
mixture #004	58.2
mixture #006	60.2

2.2. Specimens

The experimental analysis was carried out on four prismatic beams with dimensions of 15 x 15 x 70 cm^3. The beam B-Con was made of concrete without fibres (as the reference beam), while beams B-002, B-004, and B-006 were manufactured from the concrete mix containing 2 kg/m^3, 4 kg/m^3 and 6 kg/m^3 of fibres, respectively. Test specimens were stored in moulds for 24 hours at a temperature of 20 ± 2 °C, followed by subsequent storage in the chamber with humidity of 95–100 % and temperature of 20 ± 2 °C to protect them against drying. The elements were notched to induce crack formation in a specific area of the beams. The notch had a width of 4 mm and a depth of 15 mm (10 % of the beam height) and was cut on the bottom of the beam in the middle of its span. The samples were also prepared for experimental measurements by forming a speckle pattern. First, the front surfaces were coated with a white, priming coat. This treatment was necessary to even out the natural colour of the beams and to increase the contrast. After the first layer had dried, the dot patterns were applied with black spray paint to create a random pattern for the DIC.

2.3. Instrumentation and testing procedure

The 3-point bending tests were performed using testing machines equipped with a crack mouth opening displacement (CMOD) gauge extensometer 2670-130 with a base of length of 5 mm. The extensometer was inserted between two knife-edges glued to the mouth of the beam notch. The distance between the supports was 45 cm, and the preload applied to the specimen was 10 N. During the initial stage of loading, each beam was subjected to bending with a constant displacement increment of 0.3 mm/min. After the force value reached 5 kN, the beam was further loaded under the CMOD-control with a constant strain increment of 0.3 %/min. The strain was related to the base length of the extensometer, thus the absolute value of loading speed was equal to 0.015 mm/min. The test was stopped when the CMOD achieved 0.5 mm (corresponding with the strain of 10 %).

During the bending tests, the fracture process was characterized using the DIC and ultrasonic waves. Figure 3a shows the experimental setup. Photographs of the central area of the beam (covered with the speckle pattern) were taken every 5 s by a digital camera. Ultrasonic waves were also induced and measured at an interval of 5 s. Three multilayer piezoelectric transducers were used for both excitation and registration of the ultrasonic signals. They were adhered to the beams using a cyano-acrylic glue. Figure 3b illustrates the configuration of piezoelectric transducers. The actuator (A) was bonded at the centre of the left surface of the beam. Two sensors were attached to the part of the beam beyond the notch. The first sensor (S1) was situated at the centre of the right surface of the beam, while the second (S2) at the front surface of the beam, 17 cm from the beam centre in the middle of the specimen height. The motivation behind using two different sensor positions was the fact that some parts of real structures can be inaccessible. The incident wave packet was a 5-cycle sine wave with a central frequency of 80 kHz modulated by the Hanning window. The signal was created by an arbitrary waveform generator and then amplified 20 times by a high voltage amplifier. Time signals of propagating ultrasonic waves were registered by a digital oscilloscope with a sampling frequency of 8 MHz and a time duration of 5 ms.

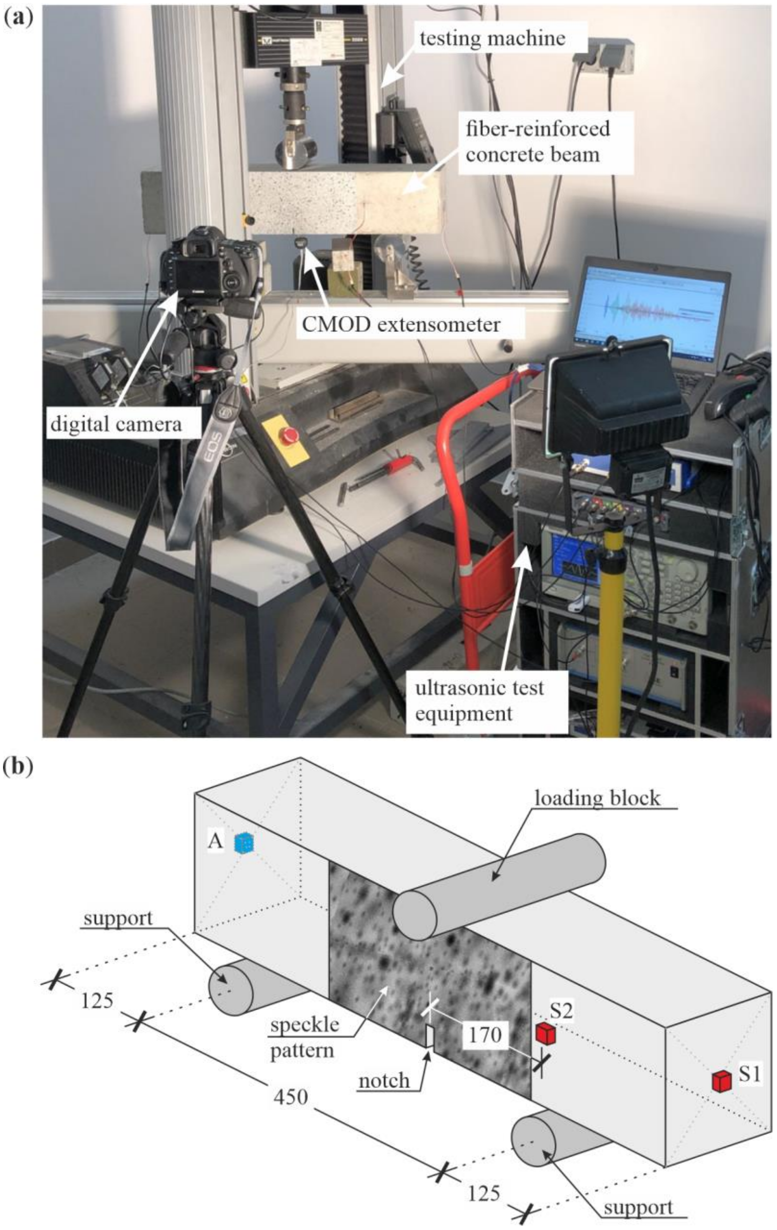

Figure 3. Experimental setup: (a) instrumentation for the bending test, UT and DIC; (b) scheme of the location of the piezoelectric actuator transducers (A – actuator, S1, S2 – sensors)

2.4. Image processing using DIC method

DIC is a commonly used non-contact optical method for tracking the displacement and strain fields. It allows the measurement of 2D or 3D coordinates based on stochastic patterns. It is important to note that 2D-DIC calculations require the photographs to be taken perpendicularly to the specimen surface. In accordance with previous literature, the edges of the specimen and the photographs are parallel and the centre of the region of interest (ROI) appears in the centre of the picture. However, there are situations when some part of the analysed object is placed behind an obstacle that makes taking photographs with the ROI situated at the central part difficult, or even impossible. In this case, the camera can be translated in parallel to the analyzed surface. The photographs are still perpendicularly taken; however, a greater area of the ROI can be registered, including the unnecessary part on the other side. In addition, the tested objects are sometimes not oriented in a precisely horizontal manner, which requires rotation of the camera in the horizontal plane. Establishing the angles of the specimen and camera can be difficult; thus, the edges of the ROI are not parallel to the edges of the picture.

In this paper, we present a procedure for the determination of strain field, and the identification and monitoring of the crack height using DIC supported with authorial pre- and post-processing scripts prepared in MATLAB®. A schematic diagram of the developed procedure is presented in Figure 4. The first step of the algorithm is the processing of digital photographs of the specimen taken during the test. The raw photographs of the surface of the objects covered with speckle pattern (Figure 4a) are firstly processed to eliminate a rigid rotation of the picture and remove unnecessary parts around the chosen ROI. With the assumption that the axes (vertical and horizontal) are equally foreshortened, these operations change the dimensions of the photographs. Thus, the scale factors along both axes are still equal. The pre-processing step described above was programmed in MATLAB® environment. As a result, rectangular photographs containing only the desired part of the element surface were obtained (Figure 4b).

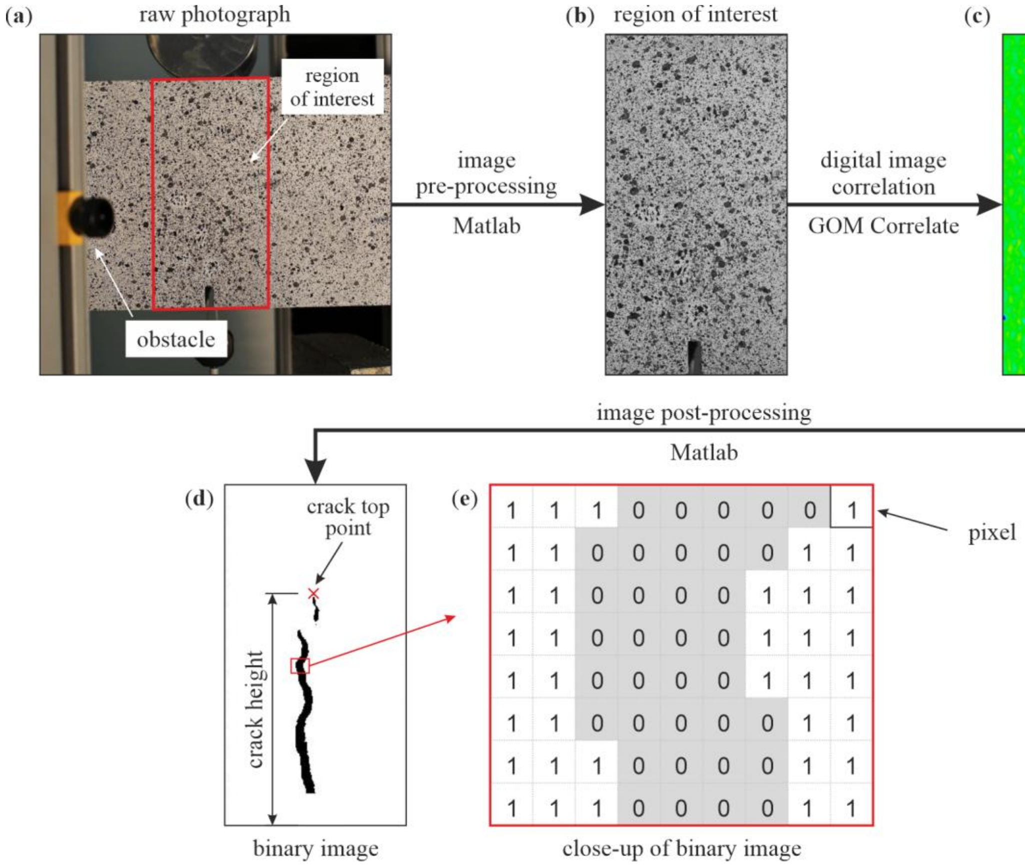

1	1	1	0	0	0	0	0	1
1	1	0	0	0	0	0	1	1
1	1	0	0	0	0	1	1	1
1	1	0	0	0	0	1	1	1
1	1	0	0	0	0	1	1	1
1	1	0	0	0	0	0	1	1
1	1	1	0	0	0	0	1	1
1	1	1	0	0	0	0	1	1

Figure 4. Schematic diagram illustrating the proposed image processing procedure for monitoring of crack development using DIC: a) raw digital photograph, b) ROI image obtained from MATLAB® pre-processing script, c) lateral strain field calculated in GOM Correlate software, d) binary image of the crack obtained from MATLAB post-processing script, e) close-up of the binary image

The prepared series of photographs were then analysed using DIC via the GOM Correlate software. DIC provides the correlation of digital images of the analysed sample, differentiating the state of deformation that needs to be determined. The assumed ROI is divided into smaller parts called facets, usually square or rectangular in shape. The accuracy of the results depends on the size of the grid obtained; the smaller the facets, the higher the resolution of the results. However, the grid size is limited by the quality of the speckle pattern. Smaller grids are sensitive to the size of the appearance of larger pattern elements. Before performing DIC calculations, scale calibration of captured images is carried out. A reference stage for zero displacements is then set, to which subsequent displacements and strains are to be compared. For typical experiments, the reference stage corresponds to the state before applying the force. During the DIC analysis, the changes in coordinates are calculated for the consecutive stages (with increasing load) in relation to the reference stage, by identifying the changes in positions of unique points in the speckle pattern. New coordinates are calculated for the pattern at each analysed stage, individually for all the consecutive images. The target subset g is then correlated with reference subset f (both M by N in size), based on the correlation coefficient calculated with respect to the equation:

$$CC^{ZMN}=\frac{\sum_{i=1}^{M}\sum_{j=1}^{N}\left[\left(f(i,j)-u_f\right)\times\left(g(i,j)-u_g\right)\right]}{\sqrt{\sum_{i=1}^{M}\sum_{j=1}^{N}\left(f(i,j)-u_f\right)^2\times\sum_{i=1}^{M}\sum_{j=1}^{N}\left(g(i,j)-u_g\right)^2}}\,. \tag{1}$$

where u_f is the intensity of the reference subset, and u_g is the intensity of the target subset [28]. The coefficient described above is calculated using the zero-mean normalized cross-correlation criterion. Using the calculated correlation, the displacement, deformation, and strain fields can be determined over the entire area of interest. In the observation of the crack evolution, lateral strain fields are determined, presenting the strain component in the direction perpendicular to the expected crack (Figure 4c).

The strain field images can be further processed to obtain an exact visualization and monitoring of the propagating crack at any consecutive step. The authorial script in MATLAB® allowed for the calculation of the change in crack height. The program converted the digital RGB pictures to binary images (Figure 4d) that show the actual shape and position of the crack. The close-up of the obtained crack image (Figure 4e) shows that any singular point, called pixel, has only one of two values: ‘zero’ for crack and ‘one’ for the rest of the points over the ROI. Thus, it can be stated that the resulting crack visualization is an M by N binary matrix. It is also important to note that the script allows the determination of crack height based on the localization of the top point of the crack (Figure 4d). This feature is useful in the observation of the crack evolution during a strength test.

2.5. Processing of wave propagation signals

The ultrasonic wave signals collected during measurements on the analysed specimens require further processing to provide clear and useful information on the level of mechanical degradation. One of the simplest indicators that may be used to detect and quantify the state of damage is to compare the metrics for determining the correspondence between two curves. For a set of ultrasonic wave signals registered at several consecutive time instances, it is assumed that the first signal is the reference, while all further signals characterize the state of damage. One of the most simple and efficient mathematical measures, based on the changes in wave amplitude and phase shift, is magnitude-phase-composite (MPC) metrics. This approach considers the curve magnitude and phase independently by the calculation of two error factors M and P, respectively. The M-error is related to the signal energy, and its value decreases with the loss of the signal amplitude. The P-error allows detection of phase shifts between the compared signals. Additionally, the comprehensive metric C can be determined as the combination of the magnitude and phase errors. The first attempt at MPC metrics was presented by Geers [41], and this proposition was further developed and applied by many researchers [24,42–44]. A popular variation of the MPC metrics was proposed by Sprague and Geers [45]. The metrics can be calculated according to the formulae:

$$M = \sqrt{\frac{\psi_{mm}}{\psi_{rr}}} - 1; \qquad P = \frac{1}{\pi}\arccos\frac{\psi_{rm}}{\sqrt{\psi_{rr}\psi_{mm}}}; \qquad C = \sqrt{M_{SG}^2 + P_{SG}^2}\,. \tag{2}$$

In the above equations, the quantities ψ_{rr}, ψ_{mm}, ψ_{rm} are determined based on the curves representing the time-domain waveforms, i.e. a reference signal $r(t)$ and a signal $m(t)$ recorded at a specific consecutive time instant during the monitoring process. For the continuous signals, the relations have the form:

$$\psi_{rr} = \frac{1}{t_2 - t_1}\int_{t1}^{t2} r^2(t)dt; \qquad \psi_{mm} = \frac{1}{t_2 - t_1}\int_{t1}^{t2} m^2(t)dt; \qquad \psi_{rm} = \frac{1}{t_2 - t_1}\int_{t1}^{t2} r(t)m(t)dt\,. \tag{3}$$

The value $t_2 - t_1$ is a range of arguments for curve comparison. If the considered signals are discretized in the time histories r_i and m_i with N samples, the integrals switch into sums, thus the above equations can be rewritten as:

$$\psi_{rr} = \frac{1}{N}\sum_{i=1}^{N} r_i^2; \qquad \psi_{mm} = \frac{1}{N}\sum_{i=1}^{N} m_i^2; \qquad \psi_{rm} = \frac{1}{N}\sum_{i=1}^{N} r_i m_i\,. \tag{4}$$

3. Results and discussion

3.1. Bending test

Figure 5 shows the load vs. CMOD relations plotted for all tested beams. It can be observed that all curves are similar in shape. The values in Table 5 allow the comparison of the curves using particular characteristics. It is clearly observable that the peak loads for all the beams were close, with mean value, standard deviation (STD) and coefficient of variation (COV) equal to 20.80 kN, 1.93 kN and 6.68 %, respectively. The corresponding positions of deformation state were also similar (mean value, STD and COV equal to 34.2 μm, 3.9 μm and 11.4 %, respectively). However, a considerable increment in ductility is visible in beams with fibres when compared with that of the beam made of plain concrete. The ductility increased with the increase in fibre dosage. A quantitative measure can be the load value at the end of the test (for CMOD equal to 0.5 mm). The notable linear correlation between the fibre content and the load at the limit can be observed, as shown in Figure 6a. The correlation coefficient for this interpolation is $r = 0.9984$). Another useful factor is the energy needed to reach the end of the test, being the integral of the force with respect to the displacement (here, the value of CMOD). The correlation between energy and fibre dose was also observed (as shown in Figure 6b, correlation coefficient $r = 0.9837$). It can be stated that the more fibre dose used in the mixture, the more energy is needed to obtain a certain displacement.

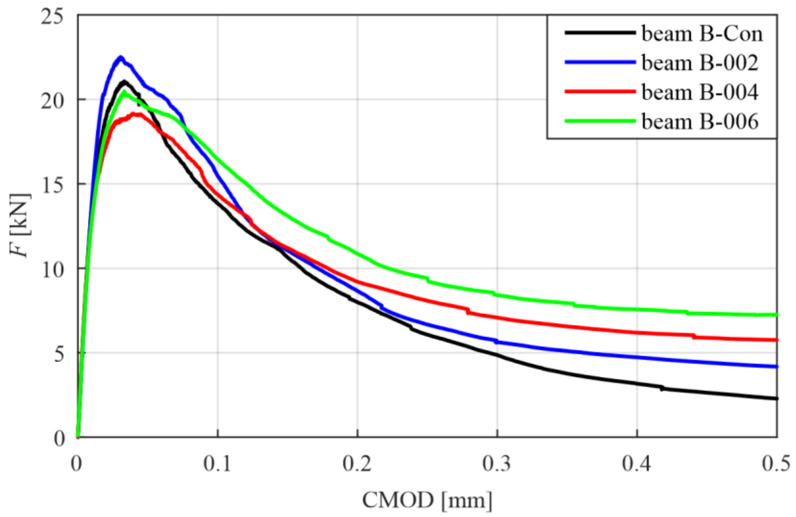

Figure 5. Fracture load–CMOD curves for tested beams

Table 5. Comparison of load vs. CMOD curves for tested beams.

Sample	Peak load [kN]	Corresponding CMOD [μm]	Load at limit [kN]	Energy [J]
B-Con	21.07	33.2	2.28	4.01
B-002	22.51	30.5	4.18	4.60
B-004	19.16	39.7	5.75	4.83
B-006	20.47	33.2	7.25	5.54

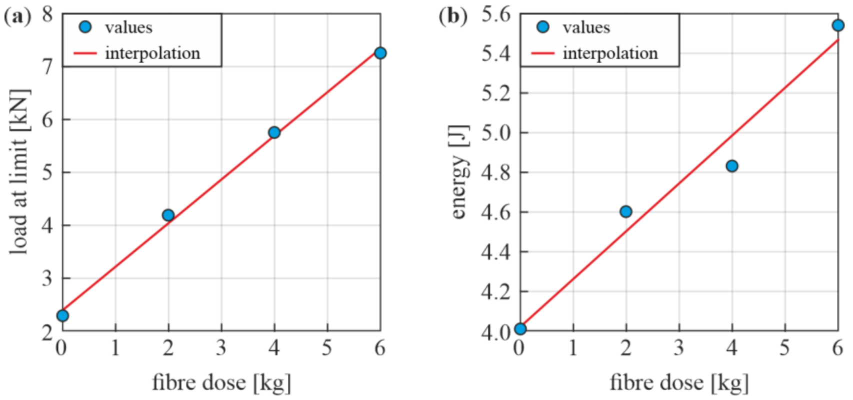

Figure 6. Influence of fibre dose on load vs. CMOD curves (functions with their linear interpolations): (a) load at limit (for CMOD = 0.5 mm) vs. fibre dose, (b) energy vs. fibre dose

3.2. DIC visualization

The crack propagation was observed by processing the photographs taken during the experiments with the proposed processing algorithm. For each beam, raw images were first cropped. Strain component maps at the surface of the specimen were then created using GOM Correlate. The quality of the obtained field was increased by adjusting the facets (size of the calculation grid). Satisfactory results were obtained for the facets of 19 pixels with 16 pixels in the point of distance. After image calibration, calculations were conducted. The engineering strains in the lateral direction (across the cracks) were determined between the undeformed stage and consecutive deformed stages. The images of the different stages of deformation are shown in Figure 7. The following steps were analyzed: at the load value equal to 90 % of the maximum force before reaching the peak value (90 % pre-$F_{\max}$), at the peak value ($F_{\max}$), at the load value equal to 90 % of the maximum force after reaching the peak value (90 % post-$F_{\max}$), and at different CMOD values equal to 0.1 mm, 0.2 mm, 0.3 mm, 0.4 mm, and 0.5 mm. These steps were selected to observe the behaviour of the crack near the peak load (to determine the moment of crack formation) and analyse the crack development over time. The analysis of individual stages allowed the tracking and monitoring of the growth and shape of the cracks. The behaviour of all the beams was similar. Clearly, the crack appeared at the peak load for beams B-Con, B-004 and B-006. In the case of beam B-002, the crack appeared later (at the stage of 90 % $F_{\max}$ after peak); however, it reached a similar height for further instances compared with other beams. These differences resulted from the fact that the crack may have arisen at the non-observed back side of the beam, and the first appearance of the crack could not have been identified. The relation between crack width and height was evident for all the specimens. With the increasing CMOD, the height of crack also increased. Notably, the beam B-Con was characterized by a cloven (double) crack. In other beams, the shape of the crack stayed single. This is due to the fact that the fibre reinforcements supported the concrete in the horizontal direction (beam B-Con, being prepared from plain concrete, did not have this support).

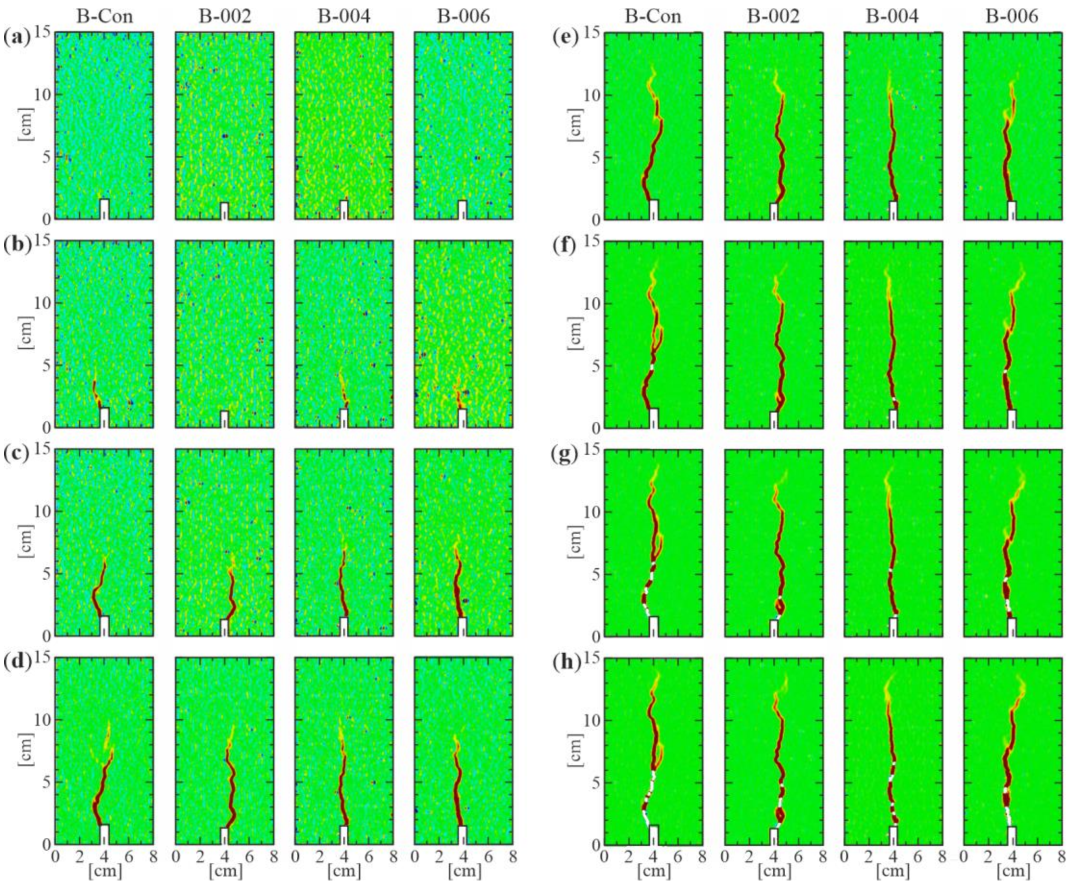

Figure 7. Lateral strain component maps (values in %) presenting the crack evolution for analysed beams at different time instances: at (a) 90 % pre-$F_{\max}$, (b) $F_{\max}$, (c) 90 % post-$F_{\max}$, (d) CMOD = 0.1 mm, (e) CMOD = 0.2 mm, (f) CMOD = 0.3 mm, (g) CMOD = 0.4 mm, (h) CMOD = 0.5 mm

It was not possible to compare the specific beams based on the above crack evolution images. A quantitative measure was needed, which was assumed to be the crack height determined by further processing of the strain fields. Figure 8 shows the dependence of the crack height and the crack opening for all beams. It can be observed that the behaviour of the cracks propagating in all beams was similar. There was no clear difference between the beams with different amounts of fibre reinforcements. At any specific stage of deformation, the crack height was similar. The cracks grew rapidly between the moment of formation and CMOD equal to 0.1 mm. After this stage, a stabilization could be observed, characterized by slower growth. It is, however, worth noting, that the crack for the beam B-Con had the greatest height for most of the stages, which may suggest lack of the fibre reinforcement.

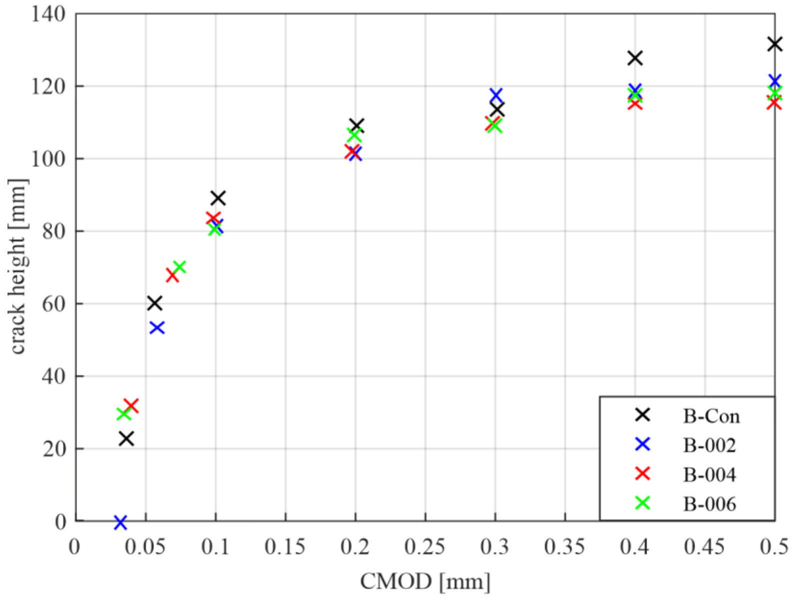

Figure 8. Relation between crack height and CMOD for all the tested beams

3.3. Ultrasonic Wave Propagation Characteristics

Figure 9 shows the representative signals collected by sensors S1 and S2 for all beams. To enhance the visibility of the time histories, the time limit of the waveforms is changed to 3.0 ms. The first and the last signals in the measurement series are presented with different colour intensities (the colour of the first signal is darker compared with that of the last one, which is lighter). There is a significant decrease in the maximum amplitudes for all time histories; thus, it can be stated that the wave energy decreases with the state of degradation. It is worth noting that the differences in the time of arrival of the first wave packets, resulting from the different distances between actuator and sensors, are visible for each beam. The time shift between signals is approximately 0.05 ms. There is no clear relation between the maximum amplitudes of signals from both sensors. For beam B-002, the maximum amplitudes are comparable. For beams B-Con and B-004, sensor S1 registered signals with greater amplitude than sensor S2, whereas for beam B-006, this relation is reversed. These differences are likely to result from the quality of the adhesive bond between the sensors and beam. Further processing of registered time histories is required to obtain efficient results. For this purpose, the signals were cut to remove the parts of signals that do not carry any useful information. The initial part of the time histories, before the appearance of the first wave packet, was cut. For sensor S1, the limit time was equal to 0.4 ms whereas for sensor S2, it was set as 0.35 ms. Then, starting with the estimated time limit, the part of the signal with a duration of 2 ms was considered in the analysis (marked in the figures).

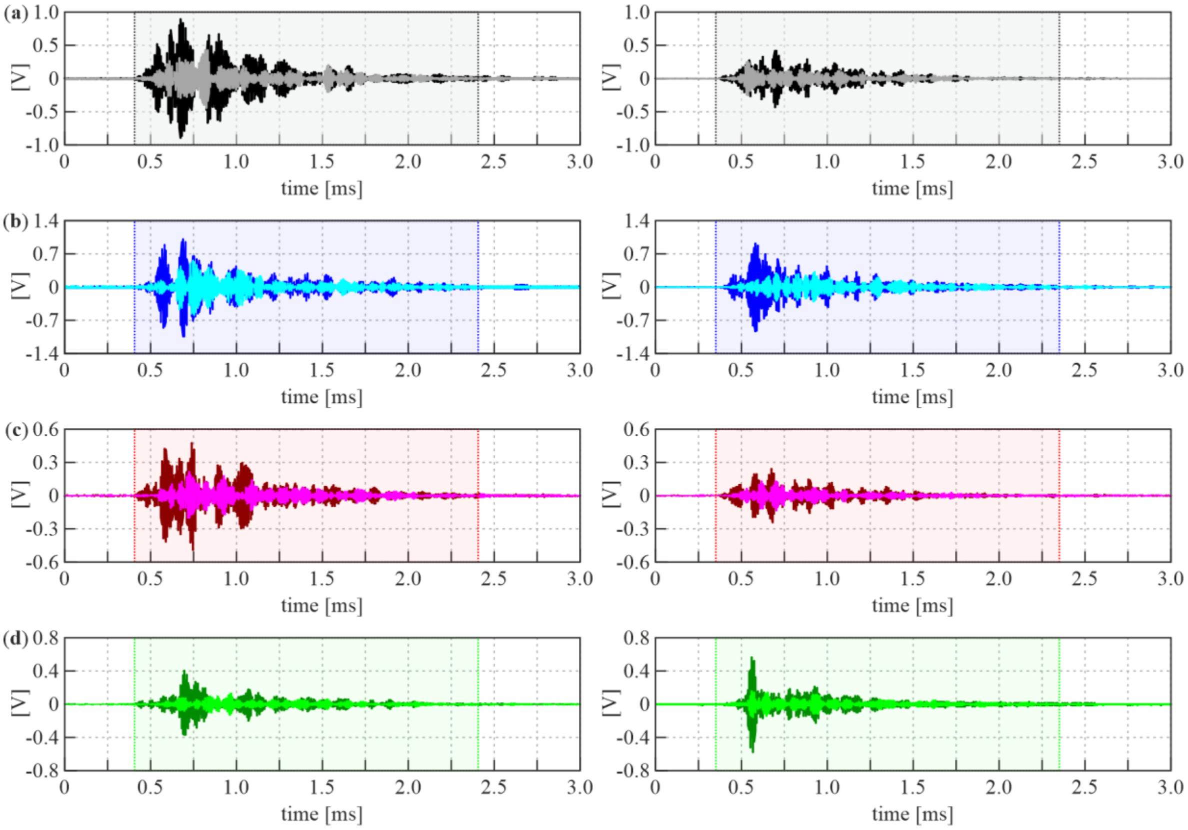

Figure 9. Ultrasonic signals collected for all beams by sensors S1 (first column) and S2 (second column): (a) B-Con, (b) B-002, (c) B-004, (d) B-006

The parts of signals presented above were processed by the calculation of MPC metrics using Sprague–Geers approach. The results of calculation of the respective metrics are presented in Figure 10, together with the load-time curves (Figure 10a) and crack height evolution curves (Figure 10e). The changes in M-error (Figure 10b) showed that the magnitude of signals from sensor S1 was almost constant at the initial stages of the bending tests for all the beams (before the maximum load value, corresponding to the crack formation, Figure 10a). For sensor S2, a slight increase in the signals can be observed for beams B-002 and B-006. After reaching the peak load value, the signal magnitude decreases with the time of degradation for both the sensors. This observation converges with the decrease in amplitude observed in the signals themselves (as shown in Figure 9). The energy loss was caused by the fact that wave energy cannot be effectively transmitted beyond the already formed crack. The crack height increases with time, which further reduces the possibility of transmission of the wave energy between the actuator and sensors. It can be stated that M-error curves were analogous to the load–time curves; however, this analogy was true only after the force peak value F_{max} was reached. A detailed comparison of both the curves for all beams and signals is presented in Figure 11. To obtain a better representation, each function was normalized in a (0,1) range. To quantify the relationship between the curves, correlation coefficients were calculated, and the corresponding values are shown above the diagrams. It is evident that the shape of load and M-error curves is similar. This agreement was confirmed by the high values of r, close to unity (most exceeding 0.96). The only exception is the M-error curve obtained for beam B-Con from sensor S2, where r significantly decreases. This effect could be a result of the disturbances in the wave propagation between the 5th and 10th minute of measurements, as the location of sensor S2 is within an easy reach of the cracking zone. For a comparison with the described analysis, the correlation coefficients for both curves in the analysed time range were calculated. The values obtained were between 0.53 and 0.75, which indicates a weak correlation. This is due to the fact that load vs. time is a monotonically increasing function, whereas M-error varies non-monotonically prior to the peak force value. The observed correlation between magnitude and load changes allows using the M-error as a first damage index (DI) in the quantitative characterization of post-peak fracture (DI_1 = M). The increasing value of DI_1 indicates progressive mechanical degradation. It can be observed that DI_1 reaching approximately 40 % corresponds to a 50 % decrease of the maximum load after the peak value; thus, it can be stated that it indicates a serious damage. However, in practice, the load cannot decrease during exploitation. Thus, considering the pre-peak behaviour of DI_1, it is not useful in monitoring of real engineering structures for early damage detection.

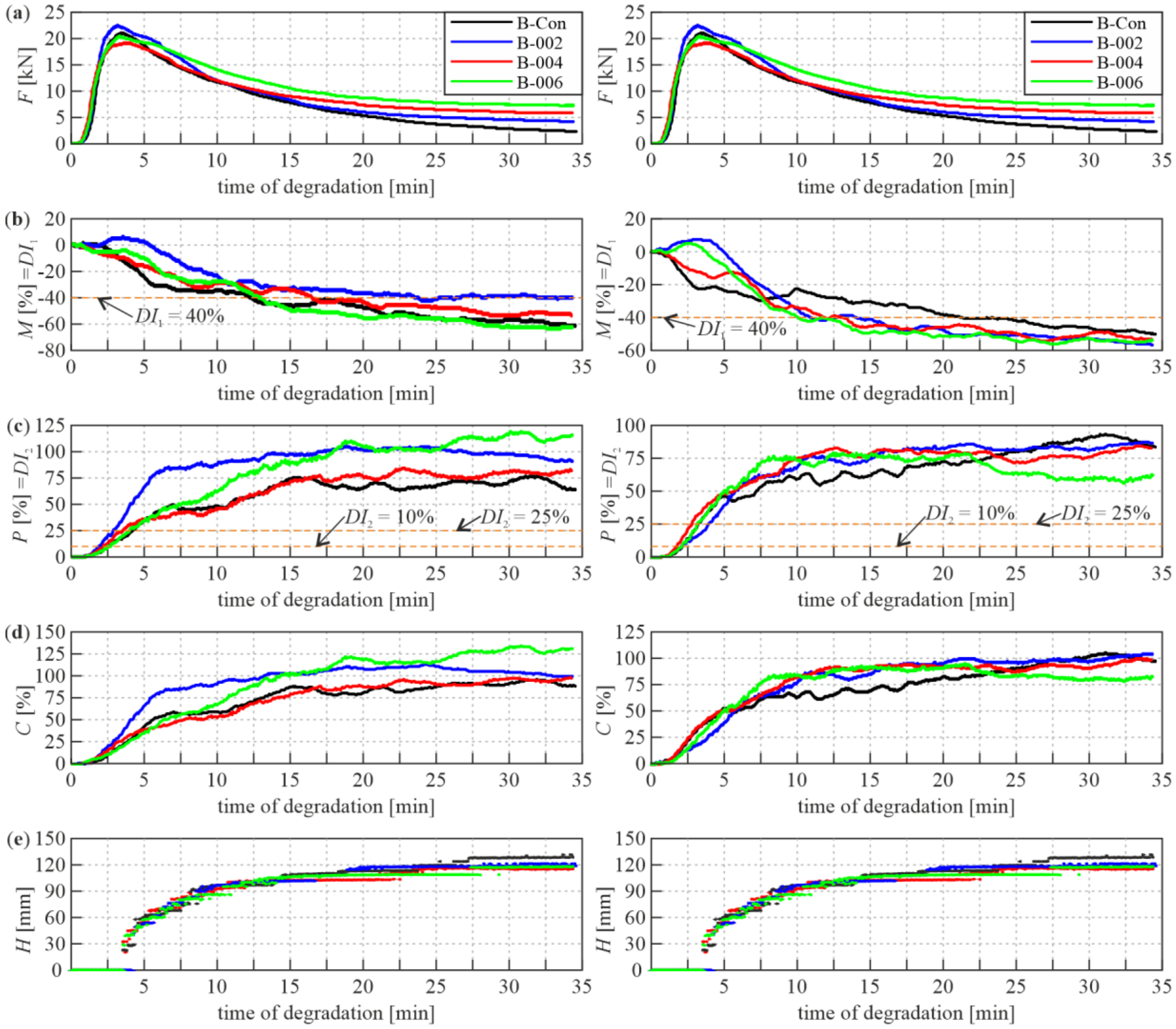

Figure 10. Magnitude-phase-composite metrics calculated for signals collected for all beams by sensors S1 (first column) and S2 (second column): (a) load-CMOD curves, (b) M-error, (c) P-error, (d) C-error, (e) evolution of crack height

Other useful observations can be made from the P-error diagrams (Figure 10c). The phase differences do not correspond with the recorded load-time curves. Interestingly, the P-error increases from the initial stages of measurements. This effect may have been caused by the stress state induced by the applied load. The value becomes stable with an increase in the time of degradation, depending on the beam and the sensor analysed. Considering sensor S1, the stabilization time was approximately 6 min for beam B-002, and approximately 15 min for the other ones. When considering sensor S2, the stabilization time can be estimated as 10 min for all the beams. It is important to note that the shape of the P-error and C-error curves corresponded with the crack height evolution curve. This resulted from the fact that the signals were significantly more shifted in time for higher cracks because the paths of the propagating waves were longer. The comparison of crack height and P-error is presented in Figure 12. The agreement of the functions was measured by calculating the correlation coefficient *r*. A strong correlation was subsequently observed (*r* exceeded 0.93). The exception is signal S2 for beam B-006, where abnormal decrease in P-error was observed after the 20th minute of measurement. This effect could result from the position of the sensor near the cracking zone, as mentioned above. Considering that P-error is strongly correlated with crack height (being a practical symptom of the potential state of damage), it could be treated as the second damage index ($DI_2 = P$). According to Figure 10c, two thresholds can be estimated. The first can be determined at DI_2 = 10 %, which corresponds to the moment when load-time curves stop being linear, and could potentially indicate the approaching damage. Another threshold is situated over DI_2 = 25 % and corresponds with the maximum load. For this moment, the damage can be advanced. Considering the fact that phase changes allowed the characterization of the pre-peak behaviour of concrete, P-error may be capable of providing information about approaching damage state prior to its significant development. The shapes of C-error curves (Figure 10d) were comparable with the P-error curves. This results from the fact that phase differences have greater influence on the composite metric than the magnitude changes. The M-errors did not exceed 60 % for both sensors, while the P-errors reached 120 % for S1 and a maximum of approximately 90 % for S2. At this stage of discussion, an important conclusion can be made based on the correlation between the crack height and P-error. The analysis of MPC metrics, the same as DIC, can be used to characterize the fracture process in fibre reinforced concrete.

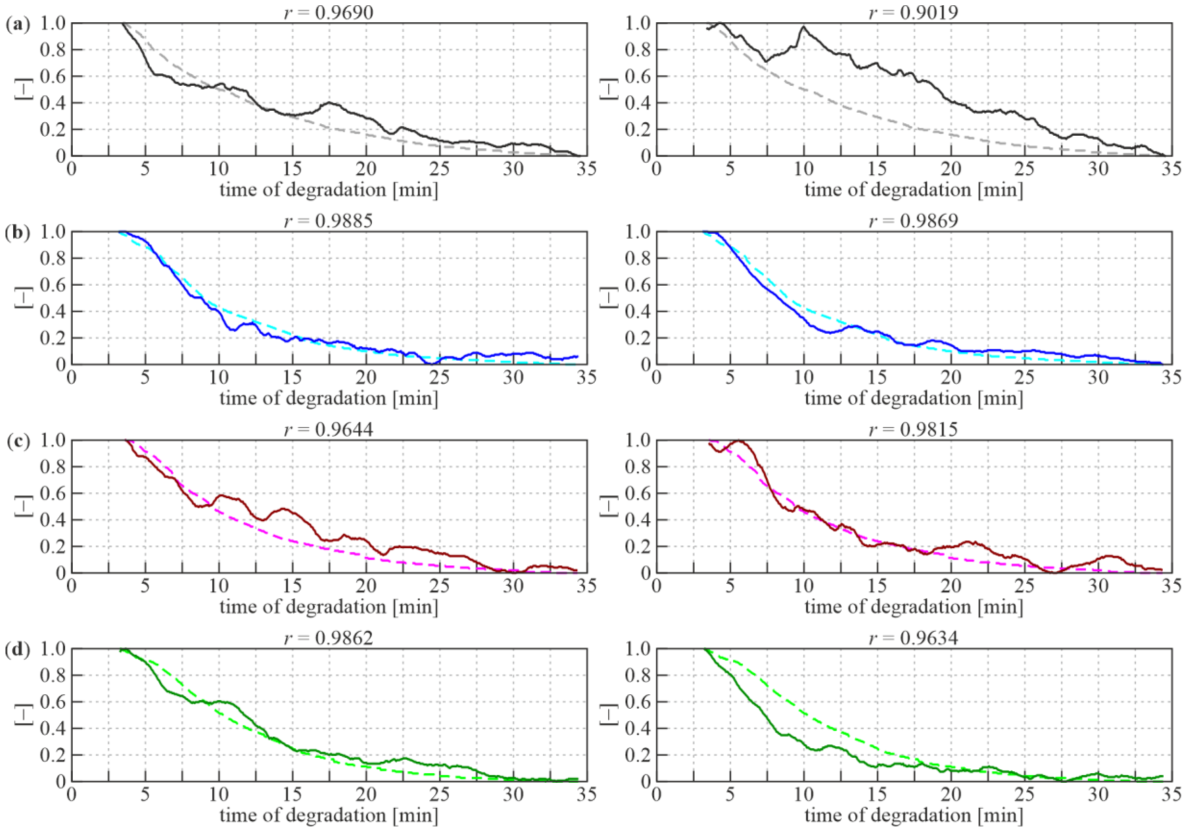

Figure 11. Correlation of load (dashed) and M-error (solid) curves (time range after reaching maximum load, normalised values) for signals collected by sensors S1 (first column) and S2 (second column) for all beams: (a) beam B-Con, (b) beam B-002, (c) beam B-004, (d) beam B-006

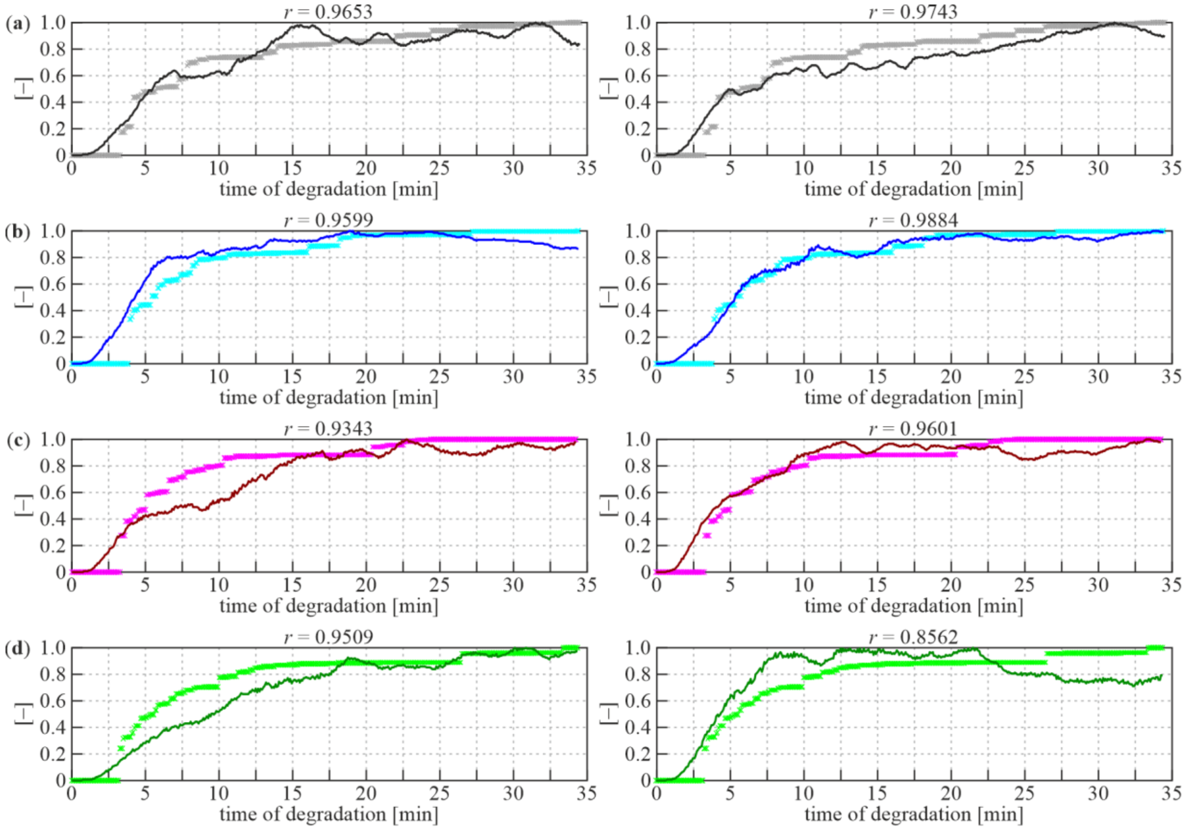

Figure 12. Correlation of crack height evolution (x-marked) and P-error (solid) curves (normalised values) for signals collected by sensors S1 (first column) and S2 (second column) for all beams: (a) beam B-Con, (b) beam B-002, (c) beam B-004, (d) beam B-006

In addition to the already presented characterization of fracture using MPC metrics, an attempt for early damage detection of cracking was made. Calculation of the function curvature was proposed as simple and powerful tool. Owing to its sensitivity to function disturbances, the curvature has many successful applications in damage detection and localization of changes in stiffness in beams and plates [46–48]. Mathematically, the curvature k of a function can be well approximated with its second derivative. Considering the characterization of P-error, it was assumed to be capable of pre-peak damage identification. The relation between the curvatures k of P-error and time (as shown in Figure 10c) was calculated by the second derivation. To enhance the results, the envelopes of the obtained curvature functions were determined. The results for all beams are presented in Figure 13. For all diagrams, there is always a single clear peak at the early stage of measurements, with an intensity of approximately 1.5–2.5. The peak starts forming when force starts increasing significantly (as shown in Figure 10a). The peak then rises and falls when the load attains maximum value (marked with a vertical line in the graphs). An exception is observed for beam B-004 (for both sensors), where the peak is doubled. This may be a result of a different shape of load curve (as shown in Figure 5). The peak load on the load-CMOD curve is reached progressively for beam B-004, unlike that for the other beams that have a single sharp tip with maximum force. According to the above presented interpretation, it may be stated that the approaching damage can be predicted if the curvature of DI_2 (P-error) rises rapidly and exceeds the value of 1 (this threshold needs to be estimated to eliminate false disturbances during the initial state of loading). If the peak load is reached and the curvature of DI_2 is decreasing, the phase error increases less rapidly and the cracks are presumed to appear. Further part of the diagrams is not useful because the rate of phase change is different for all beams. However, it is interesting to note that the shape of curvatures for the two sensors of the same beam is similar (both are simultaneously increasing or decreasing), but the amplitudes are different.

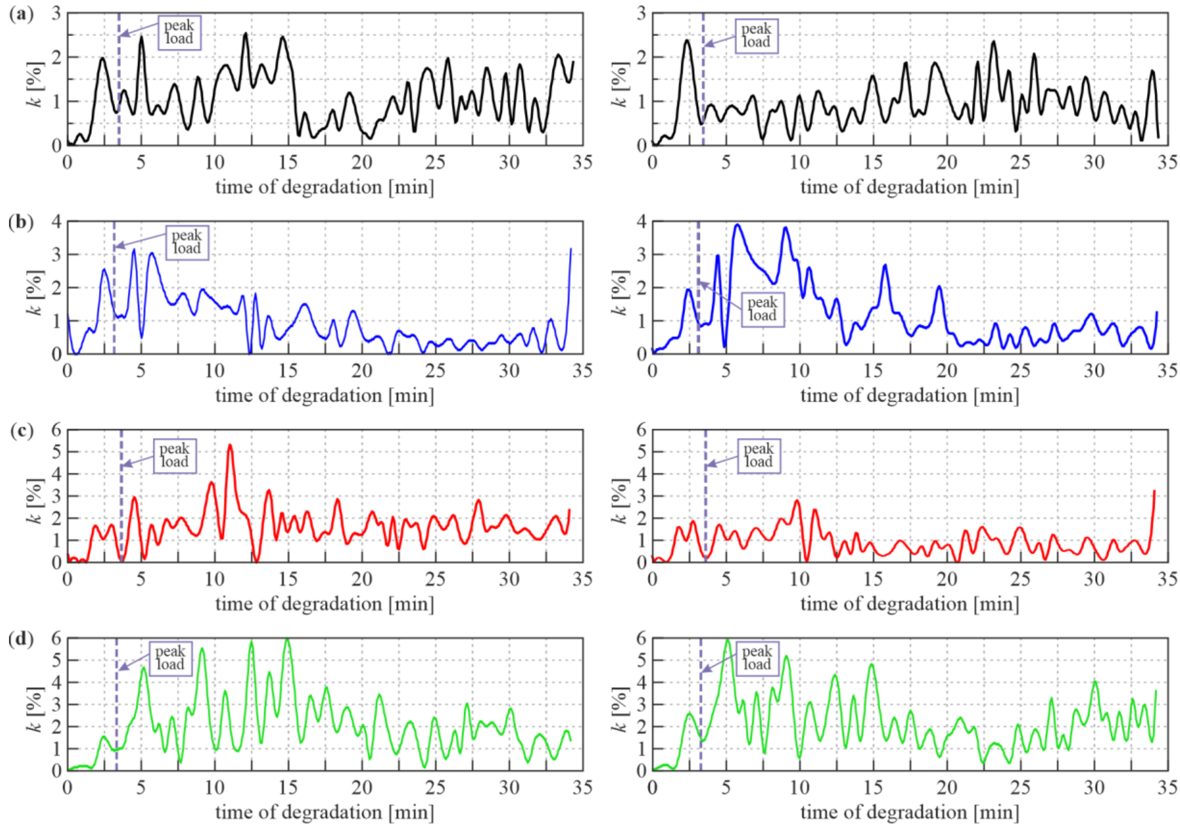

Figure 13. Curvature of P-error diagrams (with the moment of reaching the maximum load marked) for signals collected by sensors S1 (first column) and S2 (second column) for all beams: (a) beam B-Con, (b) beam B-002, (c) beam B-004, (d) beam B-006

4. Conclusions

In this paper, monitoring of the damage evolution of concrete beams and an assessment of the corresponding conditions were carried out by the integrated application of ultrasonic wave propagation and DIC techniques. A set of carefully designed experiments on fibre-reinforced concrete beams were conducted to analyse the influence of fibre dosage on the post-cracking behaviour as well as to verify the possibility of detection of cracking damages at the early stages of development.

The proposed image processing procedure for monitoring of crack development utilizes a DIC-enabled tracking of the precise crack height with changing stages of degradation. The shape of the load–CMOD curves was similar for all tested beams. Load peak values as well as the corresponding displacements of the crack opening were consistent. However, the types of mixture, differing with the fibre dosage, could be distinguished based on the load value at the post-cracking phase of bending as well as the total released energy during the fracture process. The crack in the middle of the beam grew rapidly in the initial stage of degradation, that is, for a CMOD up to 0.1 mm. Then, a slower growth occurred. The crack height for a CMOD did not change significantly with the change in volume of the fibre reinforcement. However, the beam made of the concrete without fibres had the crack with the largest height for most analysed instances. Moreover, the crack in the beam made of plain concrete had a cloven shape, which was caused by the lack of fibre reinforcement. Other beams had single cracks that were protected against branching by the fibres.

The results of the UT facilitated characterization of the state of damage based on data acquired at a limited number of points distributed on the surface of a tested element. The wave propagation technique enhanced with the calculation of the MPC metrics proved its effectiveness in identifying the state of damage at an early stage of the fracture process. Both magnitude and phase errors revealed the disturbances in signals collected during measurements; however, the differences in phase were significantly more evident.

Simultaneous registration of wave propagation signals and photographs of analysed specimens during mechanical degradation made it possible to integrate indicators of ultrasound monitoring with the crack development. It was proved that the shape of the P-error and C-error curves correspond to the shape of the crack height, while the M-error curves were analogous to the load–CMOD curves. The results of conducted investigations revealed that the energy and phase shifts of ultrasonic waves could be used in a system for the real-time monitoring of a fracture process as autonomous damage indicators. Additionally, the phase errors are promising, with scope for the early detection of degradation. In the present form, the proposed method can be effectively used to identify the existence of a crack zone. Future works will focus on advancing the presented research by considering an array of sensors and algorithms of ultrasound computed tomography to assess the location and size of the cracking zone more accurately.

Acknowledgments

The study was financed by the National Science Centre, Poland, with project No. 2019/35/B/ST8/01905.

The authors would like to thank Mr Patryk Chodkowski for the technical support during bending tests.

References

[1] E. Horszczaruk, M. Aleksandrzak, K. Cendrowski, R. Jędrzejewski, J. Baranowska, E. Mijowska, Mechanical properties cement based composites modified with nano-Fe3O4/SiO2, Constr. Build. Mater. 251 (2020) 5–10. https://doi.org/10.1016/j.conbuildmat.2020.118945.

[2] E. Horszczaruk, P. Łukowski, C. Seul, Influence of dispersing method on the quality of nano-admixtures homogenization in cement matrix, Materials (Basel). 13 (2020) 1–14. https://doi.org/10.3390/ma13214865.

[3] C. Zhuang, Y. Chen, The effect of nano-SiO2 on concrete properties: A review, Nanotechnol. Rev. 8 (2019) 562–572. https://doi.org/10.1515/ntrev-2019-0050.

[4] M. Gesoglu, E. Güneyisi, D.S. Asaad, G.F. Muhyaddin, Properties of low binder ultra-high performance cementitious composites: Comparison of nanosilica and microsilica, Constr. Build. Mater. 102 (2016) 706–713. https://doi.org/10.1016/j.conbuildmat.2015.11.020.

[5] M. Khan, M. Ali, Use of glass and nylon fibers in concrete for controlling early age micro cracking in bridge decks, Constr. Build. Mater. 125 (2016) 800–808. https://doi.org/10.1016/j.conbuildmat.2016.08.111.

[6] B. Liu, J. Guo, X. Wen, J. Zhou, Z. Deng, Study on flexural behavior of carbon fibers reinforced coral concrete using digital image correlation, Constr. Build. Mater. 242 (2020) 117968. https://doi.org/10.1016/j.conbuildmat.2019.117968.

[7] K. Turk, M. Bassurucu, R.E. Bitkin, Workability, strength and flexural toughness properties of hybrid steel fiber reinforced SCC with high-volume fiber, Constr. Build. Mater. 266 (2021) 120944. https://doi.org/10.1016/j.conbuildmat.2020.120944.

[8] M.G. Alberti, A. Enfedaque, J.C. Gálvez, On the mechanical properties and fracture behavior of polyolefin fiber-reinforced self-compacting concrete, Constr. Build. Mater. 55 (2014) 274–288. https://doi.org/10.1016/j.conbuildmat.2014.01.024.

[9] P. Pujadas, A. Blanco, S.H.P. Cavalaro, A. Aguado, S. Grünewald, K. Blom, J.C. Walraven, Plastic fibres as the only reinforcement for flat suspended slabs: Parametric study and design considerations, Constr. Build. Mater. 70 (2014) 88–96. https://doi.org/10.1016/j.conbuildmat.2014.07.091.

[10] M.G. Alberti, A. Enfedaque, J.C. Gálvez, Fracture mechanics of polyolefin fibre reinforced concrete: Study of the influence of the concrete properties, casting procedures, the fibre length and specimen size, Eng. Fract. Mech. 154 (2016) 225–244. https://doi.org/10.1016/j.engfracmech.2015.12.032.

[11] A. Mariak, M. Kurpińska, The effect of macro polymer fibres length and content on the fibre reinforced concrete, in: MATEC Web Conf., 2018: p. 03004. https://doi.org/10.1051/matecconf/201821903004.

[12] E.O. Garcez, M.I. Kabir, A. Macleod, Self-Compacting Concrete Reinforced with Twisted-Bundle Macro-Synthetic Fiber, Appl. Sci. 9 (2019) 2543. https://doi.org/10.3390/app9122543.

[13] C. Camille, D. Kahagala Hewage, O. Mirza, F. Mashiri, B. Kirkland, T. Clarke, Performance behaviour of macro-synthetic fibre reinforced concrete subjected to static and dynamic loadings for sleeper applications, Constr. Build. Mater. (2020) 121469. https://doi.org/10.1016/j.conbuildmat.2020.121469.

[14] F. Shi, T.M. Pham, H. Hao, Y. Hao, Post-cracking behaviour of basalt and macro polypropylene hybrid fibre reinforced concrete with different compressive strengths, Constr. Build. Mater. 262 (2020) 120108. https://doi.org/10.1016/j.conbuildmat.2020.120108.

[15] R.P. Manfredi, F. de Andrade Silva, Test Methods for the Characterization of Polypropylene Fiber Reinforced Concrete: A Comparative Analysis, KSCE J. Civ. Eng. 24 (2020) 856–866. https://doi.org/10.1007/s12205-020-0741-7.

[16] M. Hasani, F. Moghadas Nejad, J. Sobhani, M. Chini, Mechanical and durability properties of fiber reinforced concrete overlay: Experimental results and numerical simulation, Constr. Build. Mater. (2020) 121083. https://doi.org/10.1016/j.conbuildmat.2020.121083.

[17] Z. Yuan, Y. Jia, Mechanical properties and microstructure of glass fiber and polypropylene fiber reinforced concrete: An experimental study, Constr. Build. Mater. 266 (2021) 121048. https://doi.org/10.1016/j.conbuildmat.2020.121048.

[18] M. Szelag, Evaluation of cracking patterns in cement composites-from basics to advances: A review, Materials (Basel). 13 (2020) 2490. https://doi.org/10.3390/ma13112490.

[19] I. Iturrioz, G. Lacidogna, A. Carpinteri, Acoustic emission detection in concrete specimens: Experimental analysis and lattice model simulations, Int. J. Damage Mech. 23 (2014) 327–358. https://doi.org/10.1177/1056789513494232.

[20] S. Verbruggen, S. De Sutter, S. Iliopoulos, D.G. Aggelis, T. Tysmans, Experimental Structural Analysis of Hybrid Composite-Concrete Beams by Digital Image Correlation (DIC) and Acoustic Emission (AE), J. Nondestruct. Eval. 35 (2016) 1–10. https://doi.org/10.1007/s10921-015-0321-9.

[21] G. Lacidogna, G. Piana, F. Accornero, A. Carpinteri, Multi-technique damage monitoring of concrete beams: Acoustic Emission, Digital Image Correlation, Dynamic Identification, Constr. Build. Mater. 242 (2020) 118114. https://doi.org/10.1016/j.conbuildmat.2020.118114.

[22] F. Moradi-Marani, P. Rivard, C.P. Lamarche, S.A. Kodjo, Evaluating the damage in reinforced concrete slabs under bending test with the energy of ultrasonic waves, Constr. Build. Mater. 73 (2014) 663–673. https://doi.org/10.1016/j.conbuildmat.2014.09.050.

[23] M. Rucka, K. Wilde, Ultrasound monitoring for evaluation of damage in reinforced concrete, Bull. Polish Acad. Sci. Tech. Sci. 63 (2015) 65–75. https://doi.org/10.1515/bpasts-2015-0008.

[24] M. Rucka, Failure Monitoring and Condition Assessment of Steel-Concrete Adhesive Connection Using Ultrasonic Waves, Appl. Sci. 8 (2018) 320. https://doi.org/10.3390/app8030320.

[25] A. Deraemaeker, C. Dumoulin, Embedding ultrasonic transducers in concrete: A lifelong monitoring technology, Constr. Build. Mater. 194 (2019) 42–50.

https://doi.org/10.1016/j.conbuildmat.2018.11.013.

[26] Ł. Skarżyński, E. Syroka, J. Tejchman, Measurements and calculations of the width of the fracture process zones on the surface of notched concrete beams, Strain. 47 (2011) 319–332. https://doi.org/10.1111/j.1475-1305.2008.00605.x.

[27] J. Suchorzewski, J. Tejchman, M. Nitka, Experimental and numerical investigations of concrete behaviour at meso-level during quasi-static splitting tension, Theor. Appl. Fract. Mech. 96 (2018) 720–739. https://doi.org/10.1016/j.tafmec.2017.10.011.

[28] M. Słoński, M. Tekieli, 2D digital image correlation and region-based convolutional neural network in monitoring and evaluation of surface cracks in concrete structural elements, Materials (Basel). 13 (2020) 3527. https://doi.org/10.3390/MA13163527.

[29] Ł. Skarżyński, J. Suchorzewski, Mechanical and fracture properties of concrete reinforced with recycled and industrial steel fibers using Digital Image Correlation technique and X-ray micro computed tomography, Constr. Build. Mater. 183 (2018) 283–299. https://doi.org/10.1016/j.conbuildmat.2018.06.182.

[30] A. Picazo, J.C. Gálvez, M.G. Alberti, A. Enfedaque, Assessment of the shear behaviour of polyolefin fibre reinforced concrete and verification by means of digital image correlation, Constr. Build. Mater. 181 (2018) 565–578. https://doi.org/10.1016/j.conbuildmat.2018.05.235.

[31] V. Francioso, C. Moro, A. Castillo, M. Velay-Lizancos, Effect of elevated temperature on flexural behavior and fibers-matrix bonding of recycled PP fiber-reinforced cementitious composite, Constr. Build. Mater. (2020) 121243. https://doi.org/10.1016/j.conbuildmat.2020.121243.

[32] J. Suchorzewski, M. Prieto, U. Mueller, An experimental study of self-sensing concrete enhanced with multi-wall carbon nanotubes in wedge splitting test and DIC, Constr. Build. Mater. 262 (2020) 120871. https://doi.org/10.1016/j.conbuildmat.2020.120871.

[33] F. Suárez, L. Felipe-Sesé, F.A. Díaz, J.C. Gálvez, M.G. Alberti, On the fracture behaviour of fibre-reinforced gypsum using micro and macro polymer fibres, Constr. Build. Mater. 244 (2020). https://doi.org/10.1016/j.conbuildmat.2020.118347.

[34] D.G. Aggelis, D. V. Soulioti, E.A. Gatselou, N.M. Barkoula, T.E. Matikas, Monitoring of the mechanical behavior of concrete with chemically treated steel fibers by acoustic emission, Constr. Build. Mater. 48 (2013) 1255–1260. https://doi.org/10.1016/j.conbuildmat.2012.06.066.

[35] N.M. Barkoula, C. Ioannou, D.G. Aggelis, T.E. Matikas, Optimization of nano-silica's addition in cement mortars and assessment of the failure process using acoustic emission monitoring, Constr. Build. Mater. 125 (2016) 546–552. https://doi.org/10.1016/j.conbuildmat.2016.08.055.

[36] D. Logoń, K. Schabowicz, The recognition of the micro-events in cement composites and the identification of the destruction process using acoustic emission and sound spectrum, Materials (Basel). 13 (2020) 2988. https://doi.org/10.3390/ma13132988.

[37] M.A. Rasheed, S.S. Prakash, G. Raju, Y. Kawasaki, Fracture studies on synthetic fiber reinforced cellular concrete using acoustic emission technique, Constr. Build. Mater. 169 (2018) 100–112. https://doi.org/10.1016/j.conbuildmat.2018.02.157.

[38] D. Logoń, Identification of the destruction process in Quasi Brittle concrete with dispersed fibers based on acoustic emission and sound spectrum, Materials (Basel). 12 (2019). https://doi.org/10.3390/ma12142266.

[39] S. Rouchier, G. Foray, N. Godin, M. Woloszyn, J.J. Roux, Damage monitoring in fibre

reinforced mortar by combined digital image correlation and acoustic emission, Constr. Build. Mater. 38 (2013) 371–380. https://doi.org/10.1016/j.conbuildmat.2012.07.106.

[40] F. Zhang, G.I.Z. Garnica, Y. Yang, E. Lantsoght, H. Sliedrecht, Monitoring shear behavior of prestressed concrete bridge girders using acoustic emission and digital image correlation, Sensors (Switzerland). 20 (2020) 1–21. https://doi.org/10.3390/s20195622.

[41] T.L. Geers, Objective Error Measure for the Comparison of Calculated and Measured Transient Response Histories., Shock Vib. Bull. 54 (1984) 99–107.

[42] M.A. Sprague, T.L. Geers, Response of empty and fluid-filled, submerged spherical shells to plane and spherical, step-exponential acoustic waves, Shock Vib. 6 (1999) 147–157. https://doi.org/10.1155/1999/647090.

[43] M.A. Sprague, T.L. Geers, Spectral elements and field separation for an acoustic fluid subject to cavitation, J. Comput. Phys. 184 (2003) 149–162. https://doi.org/10.1016/S0021-9991(02)00024-4.

[44] M. Mongiardini, M.H. Ray, M. Anghileri, Acceptance criteria for validation metrics in roadside safety based on repeated full-scale crash tests, Int. J. Reliab. Saf. 4 (2010) 69–88. https://doi.org/10.1504/IJRS.2010.029565.

[45] M.A. Sprague, T.L. Geers, A spectral-element method for modelling cavitation in transient fluid-structure interaction, Int. J. Numer. Methods Eng. 60 (2004) 2467–2499. https://doi.org/10.1002/nme.1054.

[46] A.A. Pandey, M. Biswas, M.M. Samman, Damage deetection from changes in curvature mode shapes, J. Sound Vib. 145 (1991) 321–332.

[47] T.Y. Hsu, Y.C. Shih, Q.V. Pham, Damage detection of a thin plate using modal curvature via macrostrain measurement, Earthq. Eng. Eng. Vib. 18 (2019) 409–424. https://doi.org/10.1007/s11803-019-0512-y.

[48] C. Xiang, L. Li, Y. Zhou, Z. Yuan, Damage identification of beam structures based on modal curvature utility information entropy, Zhendong Yu Chongji/Journal Vib. Shock. 39 (2020) 234–244. https://doi.org/10.13465/j.cnki.jvs.2020.17.031.